



HAL
open science

High strain rate damage in porous andesite

Mai-Linh Doan, Michael Heap, Maude Schell, Ulrich Kueppers

► **To cite this version:**

Mai-Linh Doan, Michael Heap, Maude Schell, Ulrich Kueppers. High strain rate damage in porous andesite. *Journal of Volcanology and Geothermal Research*, 2022, 427, pp.107551. 10.1016/j.jvolgeores.2022.107551 . hal-03725513

HAL Id: hal-03725513

<https://hal.science/hal-03725513>

Submitted on 23 Dec 2023

HAL is a multi-disciplinary open access archive for the deposit and dissemination of scientific research documents, whether they are published or not. The documents may come from teaching and research institutions in France or abroad, or from public or private research centers.

L'archive ouverte pluridisciplinaire **HAL**, est destinée au dépôt et à la diffusion de documents scientifiques de niveau recherche, publiés ou non, émanant des établissements d'enseignement et de recherche français ou étrangers, des laboratoires publics ou privés.

1
2
3
4
5
6
7
8
9
10
11
12
13
14
15
16
17
18
19
20
21
22
23
24

High strain rate damage in porous andesite

Mai-Linh Doan^a, Michael J. Heap^{b,c}, Maude Schell^a, Ulrich Kueppers^d

^a*Univ. Grenoble Alpes, Univ. Savoie Mont Blanc, CNRS, IRD, UGE, ISTerre, 38000
Grenoble, France*

^b*Université de Strasbourg, CNRS, Institut Terre et Environnement de Strasbourg, UMR
7063, 5 rue René Descartes, Strasbourg F-67084, France*

^c*Institut Universitaire de France (IUF), Paris, France*

^d*Department of Earth and Environmental Sciences, Ludwig-Maximilians-Universität,
80333 Munich, Germany*

Abstract

25
26
27
28
29
30
31
32
33
34
35
36
37
38
39
40
41
42
43
44
45
46
47
48
49
50
51
52
53
54
55

Deformation rates at volcanoes vary enormously, potentially altering the way in which volcanic rock accommodates strain. However, relationships between deformation rate, damage patterns, and physical properties are poorly understood. Laboratory deformation experiments are typically restricted to low strain rates ($\ll 1 \text{ s}^{-1}$). Here, we deformed samples of porous andesite in compression at strain rates from 10^{-6} to $\sim 370 \text{ s}^{-1}$. We show, using X-ray computed microtomography, that the failure mode changes as a function of strain rate: macroscopic fractures form at low strain rates and samples deformed at high strain rate ($\geq 100 \text{ s}^{-1}$) contain macroscopic fractures and collapsed pores. In general, high strain rate deformation results in more pervasively damaged samples. Deformation at high strain rate also results in larger decreases and increases to P-wave velocity and permeability, respectively. Strikingly, the change in the P-wave velocity of samples deformed at high strain rate is very large (decreases of up to 50%). We hypothesize

Email address: Mai-linh.doan@univ-grenoble-alpes.fr (Mai-Linh Doan)

56
57
58
59
60
61
62
63
64
65

Preprint submitted to Journal of Volcanology and Geothermal Research February 2, 2022

1
2
3
4
5
6
7
8
9 that faster events (e.g., explosions) can shatter the adjacent host rock, which
10 could destabilise the volcano and encourage mass wasting events, increase
11 the efficiency of outgassing by increasing permeability, and increase the ash
12 content of plumes that accompany Vulcanian explosions.
13
14

15
16 *Keywords:* High strain rate damage
17
18 , Volcán de Colima, andesite, X-ray computed tomography, P-wave
19 velocity, Split Hopkinson pressure bar
20
21

22 *PACS:* 0000, 1111

23
24 *2000 MSC:* 0000, 1111
25
26

27 28 **1. Introduction**

29
30 Deformation rates at volcanoes vary tremendously, from 10^{-14} – 10^{-12} s⁻¹
31 (Owen et al., 1995; Wadge et al., 2006; Moretti et al., 2020) to strain rates
32 sufficient to fragment melt (Dingwell, 1996; Wadsworth et al., 2018) and
33 form frictional melts (Kendrick et al., 2012; Hughes et al., 2020). However,
34 the majority of laboratory deformation experiments on volcanic rocks have
35 been performed at low compressive strain rates of 10^{-5} s⁻¹ (Heap and Violay,
36 2021). Few experimental studies have focused on the strain rate dependence
37 of mechanical behavior at higher strain rates up to 10^{-1} s⁻¹ (Schaefer et al.,
38 2015; Coats et al., 2018; Lavallée et al., 2019; Heap and Violay, 2021). These
39 studies have shown that the strength of volcanic rocks increases as the strain
40 rate is increased. For example, the strength of porous dacite from Mt. Unzen
41 (Japan) increased from ~ 20 to ~ 28 MPa as the strain rate was increased from
42 10^{-5} to 10^{-1} s⁻¹ (Coats et al., 2018).
43
44
45
46
47
48
49
50
51
52
53
54

55 Experiments on granite, marble, and porous sandstone have shown that
56
57
58
59
60
61
62
63
64
65

1
2
3
4
5
6
7
8
9
10 16 rock can change failure mode at high strain rates (Aben et al., 2017a). Rather
11 17 than forming the few macroscopic fractures observed at low strain rate (\leq
12 18 10^{-1} s^{-1}), very high strain rates ($\geq 100 \text{ s}^{-1}$) pulverize low-porosity granite
13 19 (Doan and Gary, 2009) and marble (Doan and Billi, 2011) and compact
14 20 porous sandstone (Aben et al., 2017b).

15
16
17
18
19 21 It is not clear, however, whether the failure mode of volcanic rock is
20 22 similarly changed at high strain rates. For example, while Olsson (1991)
21 23 remarked that the porous tuff samples were “reduced to dust” at strain rates
22 24 of 10^3 s^{-1} , the failure of the low-porosity basalt was found to be largely
23 25 independent of strain rate (Lindholm et al., 1974). Indeed, there are very few
24 26 studies that have investigated the influence of high strain rates on the damage
25 27 evolution and failure mode of volcanic rocks. Further, while studies exist
26 28 that show that low strain rate deformation in the brittle regime ($\leq 10^{-1} \text{ s}^{-1}$)
27 29 can decrease P-wave velocities (Stanchits et al., 2006; Fortin et al., 2011)
28 30 and increase permeability of volcanic rock (Fortin et al., 2011; Farquharson
29 31 et al., 2016), corresponding data for high strain rates—important for the
30 32 monitoring and understanding of volcanic systems—do not exist.

31
32
33 33 Here, we present the results of an experimental study on the influence of
34 34 strain rate on the mechanical behavior of porous andesite. Uniaxial defor-
35 35 mation experiments were performed at strain rates from 10^{-6} to $\sim 370 \text{ s}^{-1}$.
36 36 The sample failure mode was assessed using X-ray computed microtomogra-
37 37 phy (μCT), and the P-wave velocity and permeability of select samples were
38 38 measured before and after deformation. Finally, we outline the volcanological
39 39 implications of these new data.

1
2
3
4
5
6
7
8
9
40 **2. Materials and Methods**

11
12 41 *2.1. Materials*

14 42 The andesite block used for this study was collected from the lahar de-
15
16 43 posits in the “La Lumbre” valley on the southwest flank of Volcán de Colima
17
18 44 (Mexico), a persistently-active andesitic stratovolcano located in the Trans-
19
20 45 Mexican Volcanic Belt (Varley et al., 2019). The block is the same as that
21
22 46 used in Farquharson et al. (2017). The andesite has a porphyritic texture
23
24 47 that consists of a microlite-rich groundmass that hosts phenocrysts of pla-
25
26 48 gioclase and pyroxene. The andesite contains irregularly-shaped pores and
27
28 49 microcracks.

29
30 50 Cylindrical samples, 20 mm in diameter, were cored from the block and
31
32 51 were cut and precision-ground to lengths of either 40 mm (for the ”quasi-
33
34 52 static” experiments) or 20 mm (for the ”dynamic” experiments). The con-
35
36 53 nected porosity of each sample was determined using the skeletal volume
37
38 54 measured by a helium pycnometer (an AccuPyc II pycnometer manufactured
39
40 55 by Micromeritics) and the bulk sample volume (Tab. 1).

41
42 56 *2.2. Low strain-rate testing*

44 57 The low strain rate (from 10^{-6} to 10^{-3} s $^{-1}$) “quasi-static” experiments
45
46 58 were performed at ITES (Strasbourg, France) using a uniaxial deformation
47
48 59 apparatus manufactured by Schenck and modified in-house (see schematic
49
50 60 provided in Heap et al. (2014)). Experiments were performed on dry 40 mm-
51
52 61 long samples at ambient laboratory temperatures. Axial displacement and
53
54 62 axial force were measured by a linear variable differential transducer and a

1
2
3
4
5
6
7
8
9
63 load cell, respectively. Axial displacement and axial force were converted to
10
11 axial strain and axial stress using the sample dimensions.
12
13

14
15
16
17
18
19
20
21
22
23
24
25
26
27
28
29
30
31
32
33
34
35
36
37
38
39
40
41
42
43
44
45
46
47
48
49
50
51
52
53
54
55
56
57
58
59
60
61
62
63
64
65

65 *2.3. high strain rate testing*

66 The high strain rate “dynamic” experiments were performed using a Split
67 Hopkinson Pressure Bar (SHPB) apparatus at ISTerre (Grenoble, France),
68 which can impose uniaxial strain rates between 10 to 10^3 s^{-1} (Chen and
69 Song, 2011; Gama et al., 2004). Experiments were performed on dry 20
70 mm-long samples at ambient laboratory pressures and temperatures. The
71 sample is sandwiched between two long bars, one of which is impacted by
72 a striker launched at several meters per second (Fig. 1a). Strain gauges
73 on the bars quantify the stress wave loading the sample (Fig. 1b). Stress
74 waves in elongated rod can be modelled as guided waves, the propagation of
75 which can be predicted using the Pochhammer-Chree equation (Graff, 1991).
76 The stress waves recorded in middle of the input bar and near the edge of
77 the output bar can be estimated at the edges of the bars, and hence at the
78 sample, to retrieve the first incident wave ε_i , the reflected wave ε_r , and the
79 transmitted wave ε_t . Stresses and strain rates can then be computed as

$$\sigma_i = \frac{A_b}{A_s} E (\varepsilon_i + \varepsilon_r) \quad (1)$$

$$\sigma_o = \frac{A_b}{A_s} E \varepsilon_t \quad (2)$$

$$\frac{\partial \varepsilon}{\partial t} = \frac{c}{L} (\varepsilon_i - \varepsilon_r - \varepsilon_t) \quad (3)$$

80 where E , c are the Young modulus and the elastic bar wave speed of the bar
81 material, respectively, and A_b and A_s are the cross-sectional area of the bar
82 and the sample, respectively. The stresses at the input edge (σ_i) and at the

1
2
3
4
5
6
7
8
9
10
11
12
13
14
15
16
17
18
19
20
21
22
23
24
25
26
27
28
29
30
31
32
33
34
35
36
37
38
39
40
41
42
43
44
45
46
47
48
49
50
51
52
53
54
55
56
57
58
59
60
61
62
63
64
65

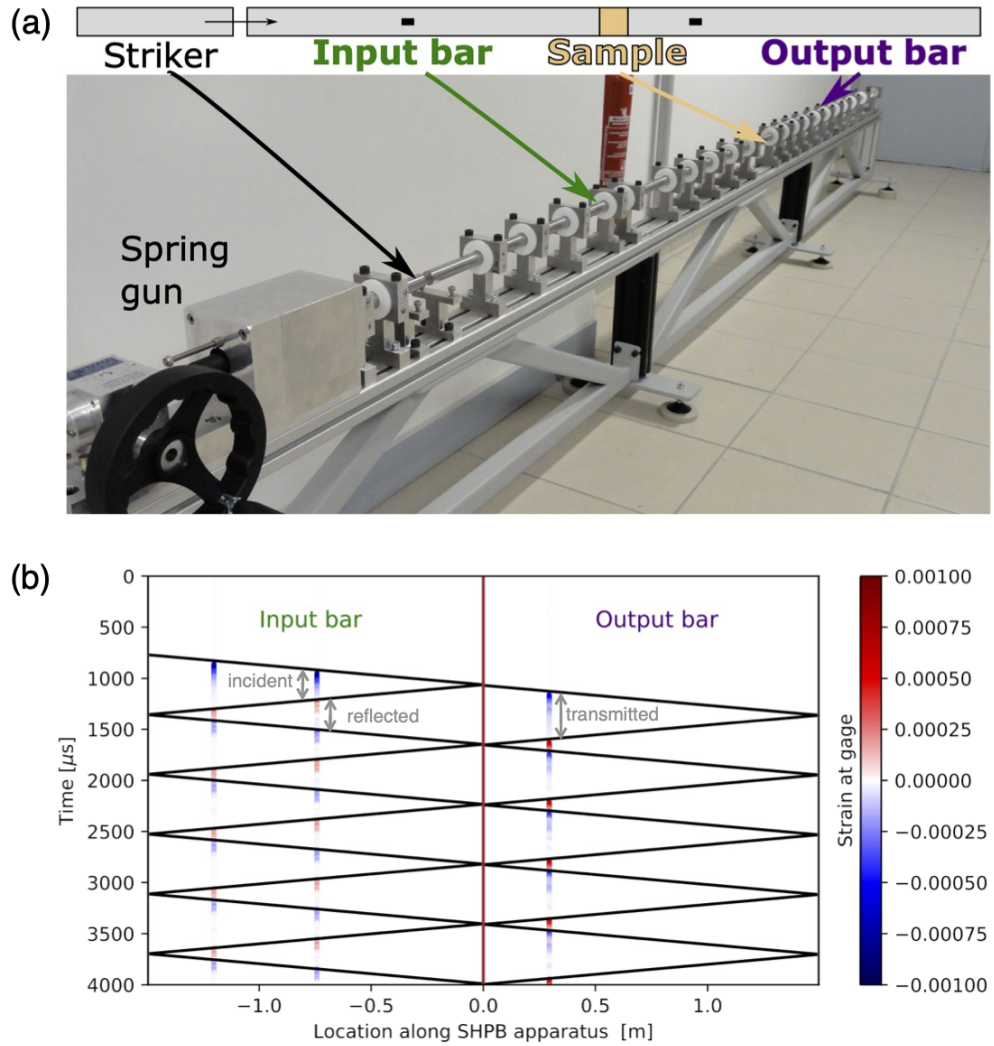


Figure 1: Split Hopkinson Pressure bars (SHPB) at ISTerre (Grenoble, France). (a) Schematics of the SHPB device and relation for the samples. (b) The four strain gauges glued along the bars (at 120 cm and 74.4 cm from the right end of the input bar, and at 29.7 cm from the left end of the output bar) record the strain wave. The wave propagation can be also modeled using 1D stress propagation. Sample is at location 0.

1
2
3
4
5
6
7
8
9 83 output edge (σ_o) are compared to check the stress equilibrium of the sample
10 84 during loading, which can be altered for strain rates or samples that are too
11 85 high or too long, respectively. Once this quality control has been performed,
12 86 the output stress is chosen as the stress acting on the sample during the test.
13 87 Strain is computed by time integrating the strain rate. Full stress-strain
14 88 curves can then be reliably retrieved (gray curves on Fig. 2).

15 89 After the first loading, the stress waves reflect perfectly at the edges of
16 90 both bars: the bars have free edges and the sample is not reloaded. The
17 91 stress-strain curves of the first loading reflects the whole loading history
18 92 on the sample. By varying the striker length, the striker speed, the pulse
19 93 shaper, and the material of the bars, a range of strain rates and stresses can
20 94 be achieved.

21 95 *2.4. X-ray imaging*

22 96 X-ray imaging was performed at ISTerre on select samples before and after
23 97 deformation. Damage patterns were assessed in two stages. In a first stage,
24 98 the deformed samples were inspected visually. The samples were classified
25 99 as either (1) intact, (2) fractured, (3) fractured with apparent compaction,
26 100 and (4) macroscopically fragmented. In a second stage, the microstructure of
27 101 select samples was investigated using μ CT to provide 3D volumes with a voxel
28 102 resolution of 15.8 μ m. This allowed us to refine our damage classifications.
29 103 A sample was classified as “fractured” when only macroscopic fractures were
30 104 visible. When some compaction was visible (pores infilled with fragments),
31 105 the sample was classified as “fractured with apparent compaction”.

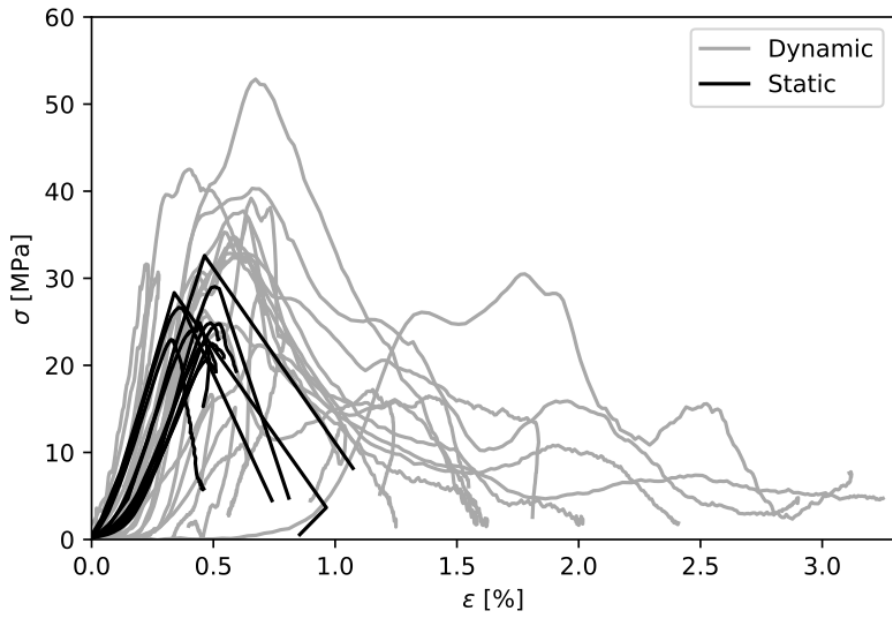


Figure 2: Strain-stress curves for andesite deformed quasi-statically (10^{-6} to 10^{-3} s^{-1} ; black curves) and dynamically (up to $\sim 370 \text{ s}^{-1}$; gray curves).

1
2
3
4
5
6
7
8
9
106 *2.5. P-wave velocity and permeability*

11
12
13
14
15
16
17
18
19
20
21
22
23
24
25
26
27
28
29
30
31
32
33
34
35
36
37
38
39
40
41
42
43
44
45
46
47
48
49
50
51
52
53
54
55
56
57
58
59
60
61
62
63
64
65

107 Damage was also assessed using petrophysical data. The P-wave velocity
108 and permeability of select samples (deformed at low and high strain rates)
109 was measured at ITES before and after deformation using a digital oscillo-
110 scope and a waveform pulse generator (see schematic provided in Heap et al.
111 (2014)) and a benchtop nitrogen permeameter (see schematic provided in
112 Heap and Kennedy (2016)), respectively. Both P-wave velocity and perme-
113 ability were measured parallel to the sample axis and at ambient laboratory
114 temperatures. Volumetric flow rates were measured for different pressure
115 differentials to calculate permeability using Darcy’s law and to check for
116 Klinkenberg and Forchheimer corrections. Due to the high permeability of
117 the studied andesite, a Forchheimer correction was applied in all cases. P-
118 wave velocity was measured at ambient pressure and permeability was mea-
119 sured under a confining pressure of 1 MPa.

120 **3. Results**

121 *3.1. Mechanical behavior at different strain rates*

122 A total of 35 experiments were performed: 15 quasi-static and 20 dynamic
123 experiments. The stress-strain curves for all experiments are provided in Fig.
124 2. The stress-strain curves for the quasi-static tests (black curves) are similar
125 to those for porous volcanic rock deformed in uniaxial compression (Heap and
126 Violay, 2021). There are no qualitative differences between the stress-strain
127 curves at strain rates between 10^{-6} to 10^{-3} s^{-1} . The stress-strain curves for
128 the dynamic tests are similar to those for the quasi-static tests, although
129 the samples deformed dynamically were typically deformed to larger strains

1
2
3
4
5
6
7
8
9
10
11
12
13
14
15
16
17
18
19
20
21
22
23
24
25
26
27
28
29
30
31
32
33
34
35
36
37
38
39
40
41
42
43
44
45
46
47
48
49
50
51
52
53
54
55
56
57
58
59
60
61
62
63
64
65

Table 1: Summary of the experimental results. “Compacted/Fractured” damage is labeled as “C/F”. Some data were not recorded and the corresponding cells are left blank.

Sample	Dimensions (mm)		Porosity (%)	V_p (m/s)		Permeability (10^{-13} m ²)		Max Strain rate (/s)	Max strain (%)	Max stress (MPa)	Damage			
	Diameter	Height		Pre	Post	Pre	Post				Macroscopic	X-ray CT scan		
SHPB	CLB1	20.06	20.47	18.23	3529	1712			196	1.13	42.6	C/F	C/F	
	CLB2	20.09	20.21	18.23	4150	3853			58	0.38	31.5	Fractured		
	CLB3	20.07	17.63	19.22	3236	3181			121	0.5	16.7	Intact		
	CLB4	20.09	18.89	22.12	3072	1660			183	1.25	32.4	C/F	C/F	
	CLB5	20.1	17.7	22.12	3106	1846			277	2.02	32.9	C/F	C/F	
	CLB6	20.08	20.74	22.36	2861	2816			138	0.59	15.2	Intact		
	CLB7	20.07	19.72	21.31	2594	1814			259	1.58	37.7	C/F	C/F	
	CLB8	20.09	19.54	17.76	2832				224	1.59	52.5	Fragmented		
	CLB9	20.08	18.61	20.49	2978	1505			369	3.23	30	C/F	C/F	
	CLB10	20.11	20	18.86	3252	2967			201	0.78	36.8	C/F	C/F	
	CLB11	20.1	20.53	22.01	2793	1251			213	2.56	32.8	C/F	C/F	
	CLB12	20.12	18.78	21.2	2867	2834			57	0.51	25.1	Intact	Fractured	
	CLB13	20.09	18.88	19.76	3120	2648			190	1.95	34.8	C/F	C/F	
	CLB14	20.1	19.46	19.22	3050	2039			259	3	40.6	C/F		
	CLB15	20.1	20.32	20.96	3040	2239	9.31	27.1	171	1.63	34.1	C/F	C/F	
	CLB16	20.05	21.6	22.99	2980				233	3.5	22.4	Fragmented		
	CLB17	20.11	20.12	17.37	2980	2668	2.76	6.22	153	0.79	38.6	Intact	C/F	
	CLB18	20.13	18.34	18.91	3160	2810			67	0.58	30.7	Fractured		
	CLB20	20.12	19.16	21.99	3250	2798			125	1.38	24	C/F		
	CLB21	20.14	18.67	21.3	3120	2110			139	1.79	26	C/F		
	Slow tests	LLB12	20.02	39.92	20.9				4.86	6.76	10^{-4}	0.74	26.6	Fractured
LLB15		20	39.75	24.15	2697	2583			10^{-5}	0.54	20.3	Fractured		
LLB18		20	40.01	21.37					10^{-4}	0.81	29	Fractured		
LLB19		20	39.99	21.07					10^{-3}	1.07	32.6	Fractured		
LLB21		20.02	39.87	20.2	2820	2509			10^{-5}	0.49	31.9	Fractured		
LLB22		19.99	39.68	21.65					10^{-6}	0.48	24.1	Fractured	Fractured	
LLB31		19.99	39.99	21.93					10^{-6}	0.46	22.9	Fractured	Fractured	
LLB34		20.02	40.01	22.23					10^{-3}	0.96	28.3	Fractured		
LLB42		19.85	39.94	25.53	2656	2351			10^{-5}	0.44	18.3	Fractured		
LLB44		20	40	20.87					10^{-5}	0.52	24.8	Fractured		
LLB46		20	40	21.72					10^{-5}	0.51	22.5	Fractured		
LLB48		19.88	39.95	26.76	2674	2579			10^{-5}	0.37	13.7	Fractured		
LLB51		20	40	21.97					10^{-5}	0.51	20.6	Fractured		
LLB52		20	40	22.4					10^{-5}	0.54	22.5	Fractured		
LLB53	19.86	39.97	25.38	2807	2531			10^{-5}	0.39	15	Fractured			

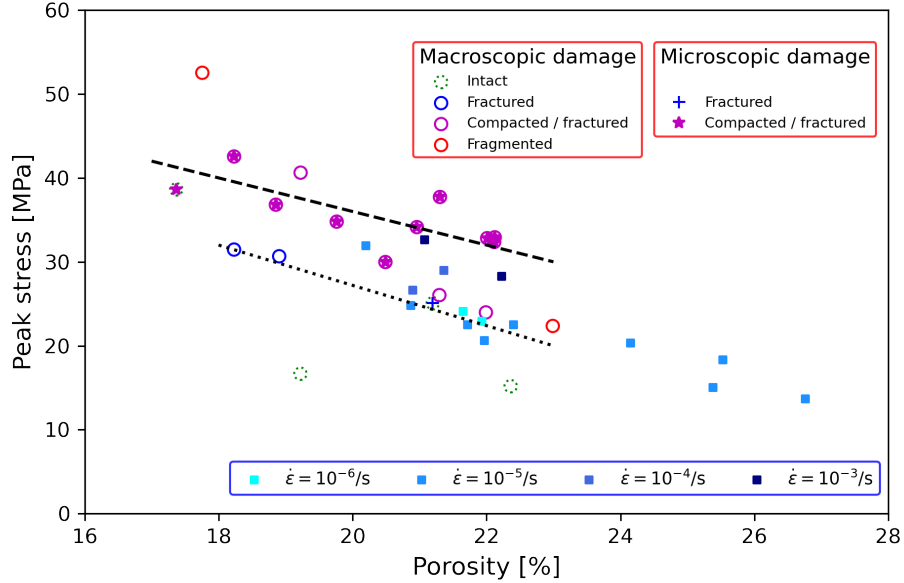


Figure 3: Influence of porosity on the peak stress of porous andesite deformed over a wide range of strain rate (10^{-6} to 10^{-3} s^{-1}).

(axial strains up to 3%, compared to 0.5-1% for the quasi-static tests, see Fig. 5b).

Fig. 3 shows the peak stress as a function of porosity for all samples (if the sample failed, the peak stress is equivalent to the uniaxial compressive strength). The strain rate is also indicated on Fig. 3. The peak stress of the samples deformed quasi-statically decreases as a function of increasing porosity, from ~ 33 MPa at a porosity of $\sim 20\%$ to ~ 13 MPa at a porosity of $\sim 26.5\%$. The relationship between peak stress and porosity is similar for the samples deformed dynamically: peak stress decreases from 53 MPa at a porosity of 18% to 20 MPa at a porosity of 22.5%. Our data extend the

1
2
3
4
5
6
7
8
9
10 140 findings of Heap and Violay (2021) and show that porosity exerts a first-order
11 141 control on the uniaxial compressive strength of the studied andesite, at all
12
13 142 strain rates (Fig. 3).

14
15 143 For a similar initial porosity (20-22%), although the strength at low-
16
17 144 strain-rate (blue squares in Fig. 3) is lower than the strength at high strain
18
19 145 rate (colored circles in Fig. 3), the influence of strain rate on strength plays
20
21 146 a second order role compared to porosity. An increase of strength as a func-
22
23 147 tion of increasing strain rate has been previously observed in low (Schaefer
24
25 148 et al., 2015; Coats et al., 2018; Lavallée et al., 2019; Heap and Violay, 2021)
26
27 149 and high (Lindholm et al., 1974; Olsson, 1991) strain rate experiments on
28
29 150 volcanic rocks, and it is typically explained in terms of the time available
30
31 151 for subcritical crack growth processes (Heap et al., 2011). However, poten-
32
33 152 tial differences in fracture patterns have not been considered so far, and are
34
35 153 discussed below.

36 37 154 *3.2. Damage at different strain rates*

38
39 155 The damage classification for each sample is presented in Fig. 5a, which
40
41 156 shows that the type of damage depends on the strain rate. All of the quasi-
42
43 157 statically deformed samples (10^{-6} and 10^{-3} s^{-1}) formed a macroscopic frac-
44
45 158 ture, a failure mode that characterizes brittle deformation. However, ap-
46
47 159 parent compaction occurred in addition to fracturing at strain rates above
48
49 160 120 s^{-1} and, at the highest strain rates, two of the samples macroscopi-
50
51 161 cally fragmented. μCT images of an intact sample, of a sample deformed
52
53 162 quasi-statically, and of three samples deformed dynamically to different axial
54
55 163 strains are shown in Fig. 4. The microstructure of the undeformed sample
56
57 164 is complex, containing irregularly shaped and heterogeneously distributed

1
2
3
4
5
6
7
8
9
10
11
12
13
14
15
16
17
18
19
20
21
22
23
24
25
26
27
28
29
30
31
32
33
34
35
36
37
38
39
40
41
42
43
44
45
46
47
48
49
50
51
52
53
54
55
56
57
58
59
60
61
62
63
64
65

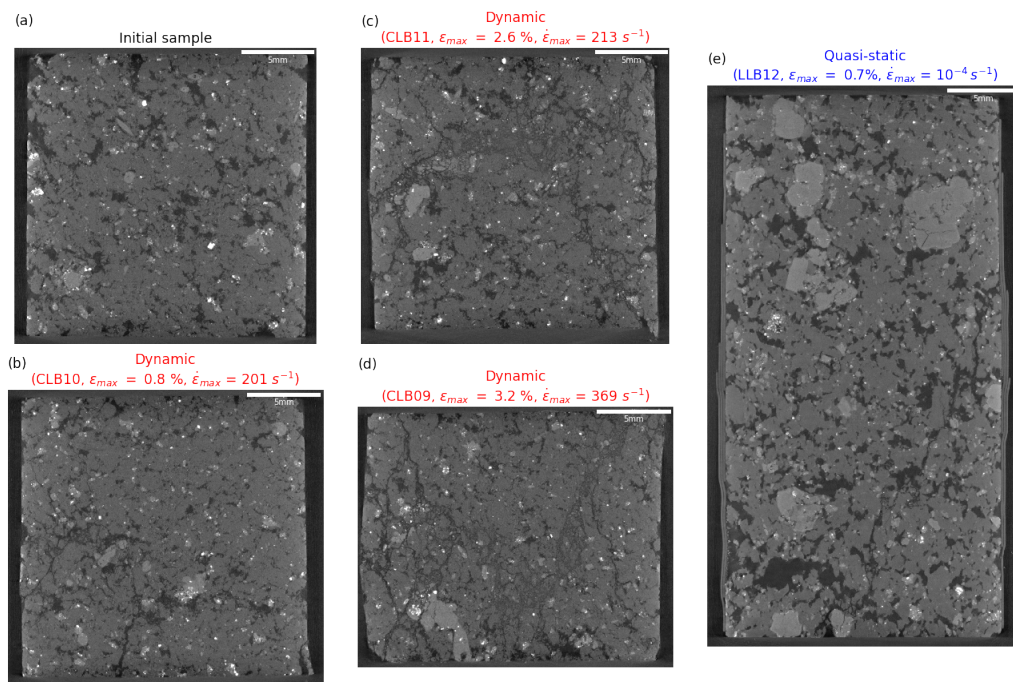


Figure 4: X-ray computed tomographic slices (black and gray represent the porosity and rock, respectively) showing an intact sample (a) of the studied andesite and the failure modes at high (b-d) and low (e) strain rate.

1
2
3
4
5
6
7
8
9
10
11
12
13
14
15
16
17
18
19
20
21
22
23
24
25
26
27
28
29
30
31
32
33
34
35
36
37
38
39
40
41
42
43
44
45
46
47
48
49
50
51
52
53
54
55
56
57
58
59
60
61
62
63
64
65

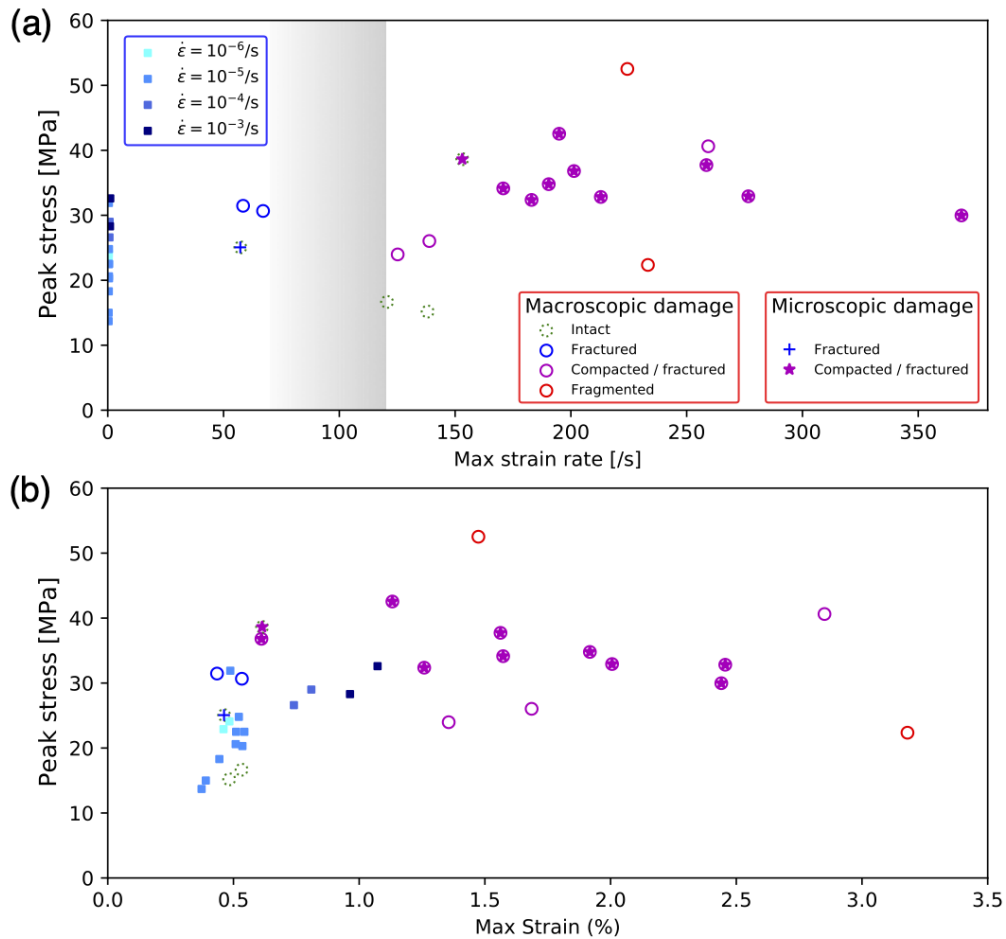


Figure 5: Influence of strain and strain-rate (panels a and b) on the peak stress of porous andesite deformed over a wide range of strain rate (10^{-6} to $10^{-3} s^{-1}$). The damage classification for the samples tested at high strain rate was determined in two phases (visual macroscopic inspection and optional μ CT imaging). All samples tested at low strain rate were fractured. Gray shade delimits the strain rate transition between fractured samples and compacted/fractured samples.

1
2
3
4
5
6
7
8
9
10 pores (as shown in 3D μ CT reconstructions of a similar andesite in Heap
11 et al. (2020)).

12
13 The quasi-statically deformed sample contains a macroscopic fracture,
14 which extends from the middle of the sample on the right-hand-side to the
15 bottom of the sample in the middle (Fig. 4). The deformation is very
16 localized in the quasi-statically deformed sample and little or no damage is
17 observed outside the macroscopic fracture.
18
19
20
21

22 The damage accumulated in the sample dynamically deformed to the
23 same axial strain is very different to the quasi-statically deformed sample
24 (Fig. 4). There is no macroscopic fracture, although some axially orientated
25 fractures are present (e.g., at the bottom of the sample in the middle) and
26 the large pores are now absent. The pores subsisting within the sample
27 are infilled with fragments. Further, pore collapse in the sample deformed
28 dynamically to an axial strain of 0.6% appears to be localized on a plane sub-
29 perpendicular to the maximum principal stress, similar to the compaction
30 bands seen previously to develop in porous volcanic rocks (Heap et al., 2015,
31 2020). The damage accumulated in the samples deformed dynamically to
32 higher axial strains (1.1 and 2.6%) is similar to that described for the quasi-
33 static sample to an axial strain of 0.6%, but much more pervasive (Fig. 4).
34
35
36
37
38
39
40
41
42
43
44

45 Samples characterised by both fracturing and compaction have a higher
46 strength than those that simply fractured (Fig. 3). This can be explained
47 by the higher fracture energy required to accommodate microfracturing and
48 grain crushing (Doan and D'Hour, 2012). To verify this, we have plotted
49 the dissipated energy $\int_0^\infty \sigma(t) \frac{\partial \epsilon(t)}{\partial t} dt$ as a function of the maximum strain
50 experienced by a sample during loading (Fig. 6). These data show that the
51
52
53
54
55
56
57
58
59
60
61
62
63
64
65

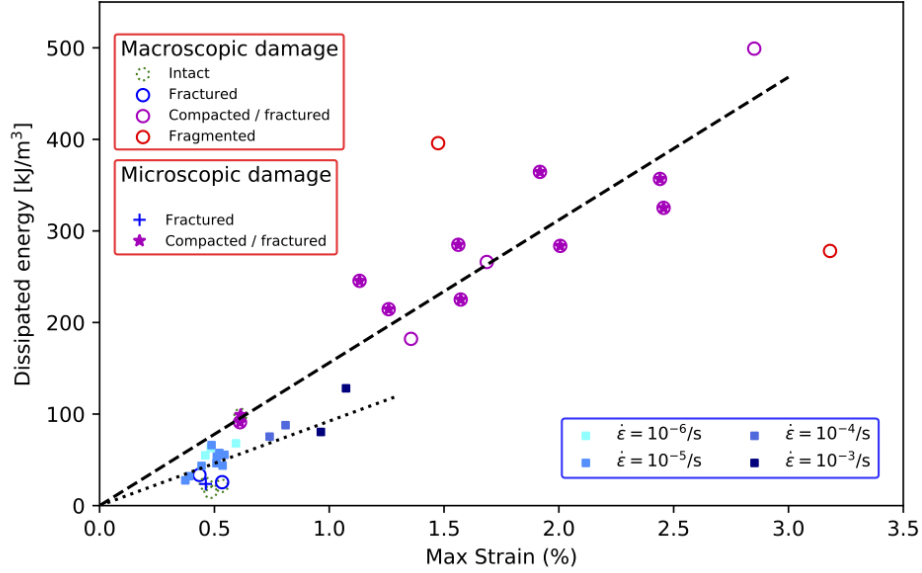


Figure 6: Increase of dissipated energy during loading as a function of strain. The samples that experience compaction/fracturing dissipate more energy than the samples who just endured fracturing.

190 samples affected by the additional compaction dissipate more energy than
 191 the samples that only endured fracturing. Since the latter type of damage
 192 only occurs above 120 s^{-1} , it offers an explanation as to why most high strain
 193 rate samples exhibit higher values of strength.

194 3.3. Change in petrophysical properties at different strain rates

195 Fig. 7 shows the relative P-wave velocity decrease as a function of porosity,
 196 strain rate, strain, and dissipated energy. The P-wave velocity decrease
 197 does not depend on the initial sample porosity (Fig. 7a), but increases as a
 198 function of increasing strain rate (Fig. 7b). P-wave velocity decrease is \leq

1
2
3
4
5
6
7
8
9
10 199 10% for the low strain samples (Fig. 7c), which also dissipated more energy
11 200 (Figs. 6 and 7d). But the P-wave velocity decrease can exceed 50% at high
12
13 201 strain (Fig. 7). It should be noted that such strains could only be achieved
14
15 202 for the damage pattern “compacted/fractured”, which is the most diffuse
16
17 203 and occurs only for the dynamic tests (Fig. 5).

18
19 204 The pre- and post-deformation permeability was also measured for sam-
20
21 205 ples deformed at a strain rates of 10^{-4} , 49, and 171 s^{-1} , respectively, and
22
23 206 showed a positive correlation of permeability increase with strain rate (Tab.
24
25 207 1). The increase in permeability following deformation is therefore higher
26
27 208 (increase of about a factor of three) for the dynamic tests than for the quasi-
28
29 209 static tests (increase of about 40%).

31 32 210 **4. Discussion and implications**

33 34 211 *4.1. Change in failure mode at higher strain rates*

35
36 212 Our data show samples accommodate strain differently at strain rates
37
38 213 above $100 - 150 \text{ s}^{-1}$, from “fractured” to “fractured with apparent com-
39
40 214 paction” (Fig. 4). The occurrence of compaction bands—planes of collapsed
41
42 215 pores connected by microcracks that formed sub-perpendicular to the max-
43
44 216 imum principal stress—has been observed during high-pressure quasi-static
45
46 217 deformation experiments on porous andesites (Heap et al., 2015, 2020). Typ-
47
48 218 ically, effective pressures of 30-40 MPa would be required to form compaction
49
50 219 bands in andesite with a similar porosity to the andesite studied here (Heap
51
52 220 et al., 2015). Dynamic loading is known to induce a dynamic confinement
53
54 221 effect, but the confining pressures generated are typically on the order of
55
56 222 5 MPa (Forrestal et al., 2007) and cannot therefore explain the presence

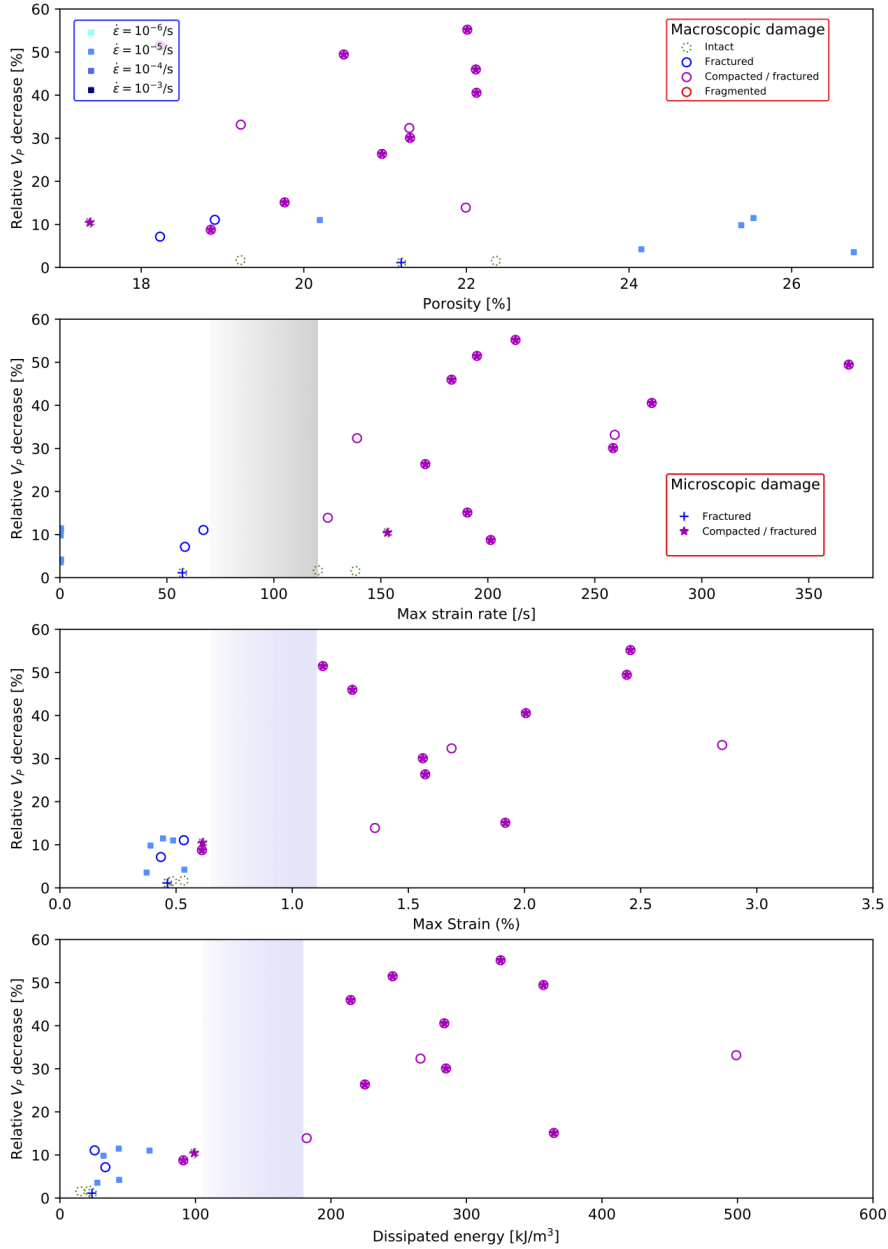


Figure 7: Relative change in P wave velocity as a function of (a) porosity, (b) strain rate, (c) strain, (d) dissipated energy.

1
2
3
4
5
6
7
8
9 223 of pore collapse during our dynamic tests (Fig. 4). Aben et al. (2017b)
10 224 showed that compaction was also observed in porous sandstone deformed
11 225 dynamically. These authors provided modeling to explain how the competi-
12 226 tion between intragranular fracturing (i.e. grain crushing) and intergranular
13 227 fracture is resolved by kinetic effects. The stress intensity factor increases
14 228 as the axial stress increases, and fracturing can occur when the stress in-
15 229 tensity factor is greater than a critical value for intragranular processes, but at higher
16 230 stresses. Intergranular fracturing (i.e. macroscopic fracture formation) is
17 231 therefore favored thermodynamically but is inhibited kinetically, explaining
18 232 why compaction can occur at higher strain rates under uniaxial conditions
19 233 (Aben et al., 2017b).

30 31 234 *4.2. Changes in petrophysical properties*

32
33 235 Our study has shown that changes to permeability and P-wave velocity
34 236 following macroscopic failure are larger at higher strain rates (Tab. 1; Fig.
35 237 7). Previous studies have shown that brittle failure in compression increases
36 238 the permeability of volcanic rock (Fortin et al., 2011; Heap et al., 2015;
37 239 Farquharson et al., 2016), and that cataclastic pore collapse decreases the
38 240 permeability of volcanic rock (Heap et al., 2015; Farquharson et al., 2017;
39 241 Heap et al., 2020). Our data show, however, that the permeability of samples
40 242 deformed at high strain rates that are “fractured with apparent compaction”
41 243 increased by about a factor of three (Tab. 1). In other words, the observed
42 244 compaction (pores infilled with fragments and possible compaction bands;
43 245 Fig. 4) did not result in a decrease in permeability and is likely the result
44 246 of presence of axially orientated fractures (Fig. 4), not present in samples
45 247 deformed quasi-statically at high pressure (Heap et al., 2015; Farquharson

1
2
3
4
5
6
7
8
9
248 et al., 2017; Heap et al., 2020). The larger increase in permeability with
10
11 increasing strain rate is likely the result of the more pervasive damage in the
12
13 samples deformed at high strain rates (Fig. 4).
14

15 A decrease in P-wave velocity following quasi-static loading to failure (Fig.
16
17 7) has been observed previously in volcanic rocks and is due to the formation
18
19 of dilatant microcracks (Stanchits et al., 2006; Fortin et al., 2011). The very
20
21 large decrease in P-wave velocity (a decrease of up to 50%) following dy-
22
23 namic loading to failure, not observed previously, is likely consequence of the
24
25 pervasively damaged and fragmented nature of the samples deformed at high
26
27 strain rate (Fig. 4). A decrease of 50% is higher than previously recorded
28
29 reductions in P-wave velocity associated with high strain rate damage. For
30
31 crystalline rocks, Aben et al. (2015) recorded P-wave velocity reductions up
32
33 to 30% for the diffuse fracturing associated with high strain rate damage.
34
35 Rempe et al. (2013) showed through subsurface seismic studies that veloc-
36
37 ities in pulverized zones of the San Andreas Fault Zone (USA) can be as
38
39 low as 1 km/s, a reduction to 20% of the expected values for the granitic
40
41 protolith.
42

243 4.3. *Volcanological implications of intense high strain rate damage*

244
245
246 The decrease in P-wave velocities after high-strain-rate loading is spec-
247
248 tacular, especially considering they were obtained on laboratory samples,
249
250 which tend to have higher P-wave velocities than those observed in the field
251
252 (Lesage et al., 2018b). Although our porous andesite samples were not pul-
253
254 verized at high strain rates (as was the case for low-porosity granites; Doan
255
256 and Gary (2009)), the significant decrease in P-wave velocity (Fig. 7) and
257
258 the pervasively damaged and fragmented nature of the samples deformed at
259
260
261
262
263
264
265
266
267
268
269
270
271
272

1
2
3
4
5
6
7
8
9 273 high-strain-rate (Fig. 4), suggests that high-strain rate damage will result
10
11 274 in a permanent decohesion that could severely weaken the rock units of the
12
13 275 volcanic edifice or the magma, both inside the conduit and above (e.g., the
14
15 276 lava dome).

16
17 277 Field measurements at Volcán de Colima show that the center of the
18
19 278 volcano exhibits similar decrease in seismic velocity at the kilometric scale,
20
21 279 extending down to 30 km (Escudero and Bandy, 2017). A decrease in P-
22
23 280 wave velocity is sometimes attributed to an increase in temperature, due
24
25 281 to the decrease in elastic wave velocities associated with thermal cracking
26
27 282 (Vinciguerra et al., 2005; Nara et al., 2011), and may indicate the presence
28
29 283 of magma. At Volcán de Colima, however, the velocity change is more intense
30
31 284 and wider in the shallow subsurface. We hypothesize that a combination of
32
33 285 repeated addition of magma into the volcanic edifice, several related heating
34
35 286 and cooling cycles, as well as the seismic energy imparted during fracture
36
37 287 opening (i.e. local) and explosive eruptions (i.e. entire edifice), resulted in
38
39 288 considerable volumes of weakened material at Volcán de Colima, and also
40
41 289 at other frequently-active stratovolcanoes worldwide. Indeed, Lesage et al.
42
43 290 (2014) found that the velocity of shallow layers of the volcano could change
44
45 291 as the waves generated by earthquakes pass through them.

46
47 292 Such weakened volcanic rock will respond differently to subsequent defor-
48
49 293 mation episodes (at any deformation rate) and could (1) mask pre-eruption
50
51 294 deformation (which was difficult to discern before the 2015 eruption at Volcán
52
53 295 de Colima; Lesage et al. (2018a)), (2) destabilize the volcanic edifice and pro-
54
55 296 mote mass wasting events (Voight and Elsworth, 1997; Borselli et al., 2011)
56
57 297 and associated hazards, (3) increase the efficiency of outgassing by increasing
58
59
60
61
62
63
64
65

1
2
3
4
5
6
7
8
9 permeability (Lavallée et al., 2013; Farquharson et al., 2015), and (4) increase
10 the ash content of eruption plumes of explosive eruptions (Webb et al., 2014).
11
12 Indeed, fragments of shattered host rock ('lithics') may be readily incorpo-
13 300 rated into the gas-particle jet of a subsequent high-energy explosive eruption.
14
15 301 Finally, increasing the permeability (Tab. 1) and the surface area available
16
17 302 for fluid-rock interactions (Fig. 4) could encourage efficient hydrothermal al-
18
19 303 teration, a process that could also further reduce the stability of the volcanic
20
21 304 flank or lava dome (Heap et al., 2021).
22
23 305

24 25 26 306 **5. Acknowledgements**

27
28
29 307 M. Heap acknowledges support from the Institut Universitaire de France
30
31 308 (IUF). T. Reuschlé and B. Renaudié are thanked for experimental assistance.
32
33 309 N. Varley and J. Farquharson are thanked for their help in collecting the
34
35 310 experimental material.

36 37 38 311 **References**

39
40
41 312 Aben, F.M., Doan, M., Gratier, J.P., Renard, F., 2017a. Coseismic Dam-
42
43 313 age Generation and Pulverization in Fault Zones: Insights From Dynamic
44
45 314 Split-Hopkinson Pressure Bar Experiments. *Geophysical Monograph* 227,
46
47 315 47–80. doi:10.1002/9781119156895.ch4.
48
49 316 Aben, F.M., Doan, M.L., Gratier, J.P., Renard, F., 2017b. High strain rate
50
51 317 deformation of porous sandstone and the asymmetry of earthquake damage
52
53 318 in shallow fault zones. *Earth and Planetary Science Letters* 463, 81–91.
54
55 319 doi:10.1016/j.epsl.2017.01.016.
56
57
58
59
60
61
62
63
64
65

- 1
2
3
4
5
6
7
8
9
320 Aben, F.M., Doan, M.L., Mitchell, T.M., Toussaint, R., Reuschlé, T., Fondri-
11 est, M., Gratier, J.P., Renard, F., 2015. Dynamic fracturing by successive
12 coseismic loadings leads to pulverization in active fault zones. *Journal*
13 of Geophysical Research: Solid Earth 121, 2338–2360. doi:Earth, 121,
14 doi:10.1002/2015JB012542.
15
16
17
18
19
325 Borselli, L., Capra, L., Sarocchi, D., De la Cruz-Reyna, S., 2011. Flank
21 collapse scenarios at Volcán de Colima, Mexico: A relative instability
22 analysis. *Journal of Volcanology and Geothermal Research* 208, 51–65.
23 doi:10.1016/j.jvolgeores.2011.08.004.
24
25
26
27
28
329 Chen, W.W., Song, B., 2011. Split Hopkinson (Kolsky) Bars. Design, Testing
30 and Applications. first edit ed., Springer, New York. doi:10.1007/978-1-
31 4419-7982-7.
32
33
34
35
36
37
38
39
40
41
42
332 Coats, R., Kendrick, J.E., Wallace, P.A., Miwa, T., Hornby, A.J., Ashworth,
33 J.D., Matsushima, T., Lavallée, Y., 2018. Failure criteria for porous dome
34 rocks and lavas: A study of Mt. Unzen, Japan. *Solid Earth* 9, 1299–1328.
35 doi:10.5194/se-9-1299-2018.
43
44
45
46
47
336 Dingwell, D.B., 1996. Volcanic dilemma : flow or blow ? *Science* 273,
337 1054–1055.
48
49
50
51
52
338 Doan, M., Billi, A., 2011. High strain rate damage of Carrara marble. *Geo-*
339 *physical Research Letters* 38. doi:10.1029/2011GL049169.
53
54
55
56
57
340 Doan, M., D’Hour, V., 2012. Effect of initial damage on rock pul-
341 verization along faults. *Journal of Structural Geology* 45, 113–124.
342 doi:10.1016/j.jsg.2012.05.006.

- 1
2
3
4
5
6
7
8
9
343 Doan, M., Gary, G., 2009. Rock pulverization at high strain rate near the
10 San Andreas fault. *Nature Geoscience* 2, 709–712. doi:10.1038/ngeo640.
11
12
13
14 345 Escudero, C.R., Bandy, W.L., 2017. Ambient seismic noise tomography of the
15 Colima Volcano Complex. *Bulletin of Volcanology* 79. doi:10.1007/s00445-
16 016-1096-2.
17
18
19
20 348 Farquharson, J., Heap, M.J., Varley, N.R., Baud, P., Reuschlé, T., 2015. Per-
21 meability and porosity relationships of edifice-forming andesites: a com-
22 bined field and laboratory study. *Journal of Volcanology and Geothermal*
23
24 350
25
26 351
27
28
29 352 Farquharson, J.I., Baud, P., Heap, M.J., 2017. Inelastic compaction and
30 permeability evolution in volcanic rock. *Solid Earth* 8, 561–581.
31
32
33
34 354 Farquharson, J.I., Heap, M.J., Baud, P., 2016. Strain-induced permeability
35 increase in volcanic rock. *Geophysical Research Letters* 43, 11,603–11,610.
36
37 356
38
39
40 357 Forrester, M.J., Wright, T.J., Chen, W.W., 2007. The effect of ra-
41 dial inertia on brittle samples during the split Hopkinson pressure
42
43 358
44 359
45
46 360
47
48
49 361 Fortin, J., Stanchits, S., Vinciguerra, S., Guéguen, Y., 2011. Influence of
50 thermal and mechanical cracks on permeability and elastic wave velocities
51
52 362
53 363
54
55 364
56
57
58
59
60
61
62
63
64
65

- 1
2
3
4
5
6
7
8
9
10 365 Gama, B.A., Lopatnikov, S.L., Gillespie, J.W., 2004. Hopkinson bar experi-
11 366 mental technique: A critical review. *Applied Mechanics Reviews* 57, 223.
12
13 367 doi:10.1115/1.1704626.
14
15
16 368 Graff, K.F., 1991. *Wave motion in elastic solids*. Dover Publications, New
17
18 369 York.
19
20 370 Heap, M., Lavallée, Y., Petrakova, L., Baud, P., Reuschle, T., Varley, N.,
21
22 371 Dingwell, D.B., 2014. Microstructural controls on the physical and me-
23
24 372 chanical properties of edifice-forming andesites at volcán de colima, mex-
25
26 373 ico. *Journal of Geophysical Research: Solid Earth* 119, 2925–2963.
27
28
29 374 Heap, M.J., Baud, P., McBeck, J.A., Renard, F., Carbillet, L., Hall, S.A.,
30
31 375 2020. Imaging strain localisation in porous andesite using digital volume
32
33 376 correlation. *Journal of Volcanology and Geothermal Research* 404, 107038.
34
35 377 doi:10.1016/j.jvolgeores.2020.107038.
36
37
38 378 Heap, M.J., Baud, P., Meredith, P.G., Vinciguerra, S., Bell, A.F., Main,
39
40 379 I.G., 2011. Brittle creep in basalt and its application to time-dependent
41
42 380 volcano deformation. *Earth and Planetary Science Letters* 307, 71–82.
43
44 381 doi:10.1016/j.epsl.2011.04.035.
45
46 382 Heap, M.J., Baumann, T.S., Rosas-Carbajal, M., Komorowski, J.C., Gilg,
47
48 383 H.A., Villeneuve, M., Moretti, R., Baud, P., Carbillet, L., Harnett, C.,
49
50 384 et al., 2021. Alteration-induced volcano instability at la soufrière de guade-
51
52 385 loupe (eastern caribbean). *Journal of Geophysical Research: Solid Earth*
53
54 386 126, e2021JB022514.
55
56
57
58
59
60
61
62
63
64
65

- 1
2
3
4
5
6
7
8
9
387 Heap, M.J., Farquharson, J., Baud, P., Lavallée, Y., Reuschlé, T., 2015.
10
11 Fracture and compaction of andesite in a volcanic edifice. *Bulletin of*
12
13 389 *Volcanology* 77. doi:10.1007/s00445-015-0938-7.
14
15
16 390 Heap, M.J., Kennedy, B.M., 2016. Exploring the scale-dependent perme-
17
18 391 ability of fractured andesite. *Earth and Planetary Science Letters* 447,
19
20 392 139–150.
21
22 393 Heap, M.J., Violay, M.E., 2021. The mechanical behaviour and failure modes
23
24 394 of volcanic rocks: a review. *Bulletin of Volcanology* 83. doi:10.1007/s00445-
25
26 395 021-01447-2.
27
28
29 396 Hughes, A., Kendrick, J.E., Salas, G., Wallace, P.A., Legros, F., Di Toro,
30
31 397 G., Lavallee, Y., 2020. Shear localisation, strain partitioning and frictional
32
33 398 melting in a debris avalanche generated by volcanic flank collapse. *Journal*
34
35 399 *of Structural Geology* 140, 104132.
36
37
38 400 Kendrick, J.E., Lavallée, Y., Ferk, A., Perugini, D., Leonhardt, R., Dingwell,
39
40 401 D.B., 2012. Extreme frictional processes in the volcanic conduit of mount
41
42 402 st. helens (usa) during the 2004-2008 eruption. *Journal of Structural Ge-*
43
44 403 *ology* 38, 61–76. doi:10.1016/j.jsg.2011.10.003.
45
46 404 Lavallée, Y., Benson, P.M., Heap, M.J., Hess, K.U., Flaws, A., Schillinger,
47
48 405 B., Meredith, P.G., Dingwell, D.B., 2013. Reconstructing magma failure
49
50 406 and the degassing network of dome-building eruptions. *Geology* 41, 515–
51
52 407 518.
53
54 408 Lavallée, Y., Heap, M.J., Kendrick, J.E., Kueppers, U., Donald B. Dingwell,
55
56 409 2019. The fragility of volcán de colima—a material constraint, in: Varley,

- 1
2
3
4
5
6
7
8
9
410 N.R., Connor, C.B., Komorowski, J.C. (Eds.), Volcán de Colima. Springer,
11 pp. 241–266. doi:10.1007/978-3-642-25911-1_7.
12
13
412 Lesage, P., Carrara, A., Pinel, V., Arámbula-Mendoza, R., 2018a. Absence
15 of Detectable Precursory Deformation and Velocity Variation Before the
16 Large Dome Collapse of July 2015 at Volcán de Colima, Mexico. *Frontiers*
17 in Earth Science 6, 1–12. doi:10.3389/feart.2018.00093.
18
19
20
21
416 Lesage, P., Heap, M.J., Kushnir, A., 2018b. A generic model for the shallow
23 velocity structure of volcanoes. *Journal of Volcanology and Geothermal*
24 Research 356, 114–126. doi:10.1016/j.jvolgeores.2018.03.003.
25
26
27
28
419 Lesage, P., Reyes-Dávila, G., Arámbula-Mendoza, R., 2014. Large tectonic
30 earthquakes induce sharp temporary decreases in seismic velocity in Volcán
31 de Colima, Mexico. *Journal of Geophysical Research: Solid Earth* 119,
32 4360–4376. doi:10.1002/2013JB010884.
33
34
35
36
37
423 Lindholm, U.S., Yeakley, L.M., Nagy, A., 1974. The dynamic strength and
38 fracture properties of dresser basalt. *International Journal of Rock Me-*
39 *chanics and Mining Sciences* 11, 181–191. doi:10.1016/0148-9062(74)90885-
40 7.
41
42
43
44
45
46
47
48
49
50
51
52
53
54
55
56
432 Moretti, R., Komorowski, J.C., Ucciani, G., Moune, S., Jessop, D., de Cha-
balier, J.B., Beauducel, F., Bonifacie, M., Burtin, A., Vallée, M., Der-
oussi, S., Robert, V., Gibert, D., Didier, T., Kitou, T., Feuillet, N.,
Allard, P., Tamburello, G., Shreve, T., Saurel, J.M., Lemarchand, A.,
Rosas-Carbajal, M., Agrinier, P., Le Friant, A., Chaussidon, M., 2020.
The 2018 unrest phase at La Soufrière of Guadeloupe (French West In-

- 1
2
3
4
5
6
7
8
9
10 433 dies) andesitic volcano: Scrutiny of a failed but prodromal phreatic erup-
11 434 tion. *Journal of Volcanology and Geothermal Research* 393, 106769.
12 435 doi:10.1016/j.jvolgeores.2020.106769.
- 13
14
15 436 Nara, Y., Meredith, P.G., Yoneda, T., Kaneko, K., 2011. Influence of macro-
16 437 fractures and micro-fractures on permeability and elastic wave velocities
17 438 in basalt at elevated pressure. *Tectonophysics* 503, 52–59.
- 18
19
20
21
22 439 Olsson, W.A., 1991. The compressive strength of tuff as a function of strain
23 440 rate from 10^{-6} to 10^3 /s. *International Journal of Rock Mechanics and*
24 441 *Mining Sciences* 28, 115–118. doi:10.1016/0148-9062(91)93241-W.
- 25
26
27
28 442 Owen, S.E., Segall, P., Freymueller, J., Mikijus, A., Denlinger, R., Ar-
29 443 nadóttir, T., Sako, M., Bürgmann, R., 1995. Rapid deformation of
30 444 the south flank of Kilauea volcano, Hawaii. *Science* 267, 1328–1332.
31 445 doi:10.1126/science.267.5202.1328.
- 32
33
34
35
36
37 446 Rempe, M., Mitchell, T.M., Renner, J., Nippres, S., Ben-Zion, Y., Rockwell,
38 447 T.K., 2013. Damage and seismic velocity structure of pulverized rocks near
39 448 the San Andreas Fault. *Journal of Geophysical Research: Solid Earth* 118,
40 449 2813–2831. doi:10.1002/jgrb.50184.
- 41
42
43
44
45 450 Schaefer, L.N., Kendrick, J.E., Oommen, T., Lavallée, Y., Chigna, G., 2015.
46 451 Geomechanical rock properties of a basaltic volcano. *Frontiers in Earth*
47 452 *Science* 3, 1–15. doi:10.3389/feart.2015.00029.
- 48
49
50
51
52 453 Stanchits, S., Vinciguerra, S., Dresen, G., 2006. Ultrasonic velocities, acous-
53 454 tic emission characteristics and crack damage of basalt and granite. *Pure*
54 455 *and Applied Geophysics* 163, 974–993. doi:10.1007/s00024-006-0059-5.
- 55
56
57
58
59
60
61
62
63
64
65

1
2
3
4
5
6
7
8
9
10
11
12
13
14
15
16
17
18
19
20
21
22
23
24
25
26
27
28
29
30
31
32
33
34
35
36
37
38
39
40
41
42
43
44
45
46
47
48
49
50
51
52
53
54
55
56
57
58
59
60
61
62
63
64
65

456 Varley, N.R., Connor, C.B., Komorowski, J.C. (Eds.), 2019. Volcán de Col-
457 ima. Springer, Heidelberg. doi:10.1007/978-3-642-25911-1.

458 Vinciguerra, S., Trovato, C., Meredith, P.G., Benson, P.M., 2005. Relating
459 seismic velocities, thermal cracking and permeability in mt. etna and ice-
460 land basalts. International Journal of Rock Mechanics and Mining Sciences
461 42, 900–910.

462 Voight, B., Elsworth, D., 1997. Failure of volcano slopes. Geotechnique 47,
463 1–31.

464 Wadge, G., Mattioli, G.S., Herd, R.A., 2006. Ground deformation at
465 Soufrière Hills Volcano, Montserrat during 1998-2000 measured by radar
466 interferometry and GPS. Journal of Volcanology and Geothermal Research
467 152, 157–173. doi:10.1016/j.jvolgeores.2005.11.007.

468 Wadsworth, F.B., Witcher, T., Vossen, C.E., Hess, K.U., Unwin, H.E., Scheu,
469 B., Castro, J.M., Dingwell, D.B., 2018. Combined effusive-explosive silicic
470 volcanism straddles the multiphase viscous-to-brittle transition. Nature
471 communications 9, 1–8.

472 Webb, E.B., Varley, N.R., Pyle, D.M., Mather, T.A., 2014. Thermal imaging
473 and analysis of short-lived Vulcanian explosions at Volcán de Colima, Mex-
474 ico. Journal of Volcanology and Geothermal Research 278-279, 132–145.
475 doi:10.1016/j.jvolgeores.2014.03.013.